ADVANCED MATERIALS INTERFACES
Open Access
www.advmatinterfaces.de

Integration of Metal Meshes as Transparent Conducting Electrodes into Perovskite Solar Cells

Chiara Ongaro, Bart Roose, Jeremy Fleury, René Schneider, Kyle Frohna, Zher Ying Ooi, Jakob Heier, Samuel D. Stranks, and Andreas Schüler*

As the demand for photovoltaic technologies continues to grow, the quest for efficient and sustainable transparent conducting electrodes (TCEs) rapidly rises. Traditional solutions, such as indium tin oxide (ITO), face challenges related to indium scarcity and environmental impact. To tackle these issues, a novel metal mesh rear TCE consisting of gold micro-meshes is developed as ITO replacement in perovskite solar cells (PSCs). This study reveals that optimized Au meshes can guarantee 75% of the extracted photocurrent compared to reference devices with ITO and a promising power conversion efficiency (PCE) of 8.65%. By utilizing hybrid mesh structures with a 10-nm ITO layer, the PCE further improves to 12.1%, with the extracted current exceeding 80% of the reference. Metal meshes can even serve to replace the opaque metal contact of PSCs, amplifying their functionality and efficiency through bifacial and multi-junction applications. Here, aerosol jet-printed silver meshes serve as front electrodes, combined with either 5–10 nm of Au, achieving efficient semi-transparent devices (PCE 16.8%), or with 5–10 nm of ITO, providing enhanced bifacial properties while maintaining competitive efficiency. Overall, this work highlights remarkable features of metal meshes, making them promising alternatives to commonly used TCEs in optoelectronic applications.

1. Introduction

Perovskite solar cells (PSCs) have emerged as highly attractive solutions to pave the way for cost reductions in photovoltaic (PV) technologies and continued advancements in efficiency. With the cost of silicon modules being pinned by the balance of system costs[1] and the cells' lab efficiencies nearing their theoretical limits,[2,3] exclusivity of silicon solar cells might no longer be a foregone conclusion for a rapid deployment of PV technologies. According to the International Energy Agency, PV installations should approach 1 TW per year to meet the 1.5 °C objective. To put this into perspective, the current cumulative PV installations amount to 1 TW, making it one of the most significant challenges of our time.[4,5]

PSCs present remarkable optoelectronic properties, low raw material cost, potential for a short energy payback time, and relatively simple synthesis processes.[6–9] However, despite significant progress in their development, several obstacles still hinder their full potential. Notably, scalability is a crucial challenge that must be addressed to facilitate the transition from current lab-scale manufacturing techniques to larger-area devices. Currently, up-scaling is coupled with performance losses primarily stemming from the increase of sheet resistance in the conducting electrodes as their dimensions increase. The identification of suitable materials and manufacturing methods for conducting electrodes represents a pivotal challenge that must be addressed to facilitate the market entry of PSCs.[9,10]

For nearly four decades, the quest for effective transparent conducting electrodes (TCEs) has primarily revolved around doped metal oxides, with a strong emphasis on indium tin oxide (ITO).[11] While this material offers high electrical conductivity and good transmittance in the visible range, it also presents major drawbacks. Notably, the US Department of Energy has classified ITO as a critical material due to its scarcity and high demand, resulting in a high supply risk for the industry.[12] ITO has also been identified as a hotspot in the life cycle analysis of perovskite modules. Gong et al. reported that both in terms of energy intensity (MJ m^{-2} per module) and carbon footprint ($kgCO_2$-eq m^{-2} per module), ITO is responsible for about 80% of the module's impact.[13] Furthermore, ITO is inherently brittle, rendering it unsuitable for flexible device applications.[14]

C. Ongaro, J. Fleury, A. Schüler
ENAC IIC Renewable Energies Cluster
Station 18 - GC A0 392, CH-1015Lausanne, Switzerland
E-mail: chiara.ongaro@epfl.ch
C. Ongaro, B. Roose, K. Frohna, Z. Y. Ooi, S. D. Stranks
Department of Chemical Engineering and Biotechnology
University of Cambridge
Philippa Fawcett Drive, Cambridge CB3 0AS, UK
R. Schneider, J. Heier
EMPA
Swiss Federal Laboratories for Materials Science and Technology
Überlandstrasse 129, CH-8600 Dübendorf, Switzerland

The ORCID identification number(s) for the author(s) of this article can be found under https://doi.org/10.1002/admi.202300923

© 2023 The Authors. Advanced Materials Interfaces published by Wiley-VCH GmbH. This is an open access article under the terms of the Creative Commons Attribution License, which permits use, distribution and reproduction in any medium, provided the original work is properly cited.

DOI: 10.1002/admi.202300923

Ongoing research is actively seeking alternatives to address the challenges associated with ITO in optoelectronic devices and guaranteeing a sustainable industry at the terawatt scale.[15] Some notable options include materials like alternative transparent conducting oxides (TCOs), metal films, carbon nanotubes, nanowires, graphene flakes, and especially, metal meshes.[16,17] Among those, metal meshes offer a highly promising solution due to their exceptional combination of low sheet resistance, high transparency, and mechanical flexibility. Their outstanding properties establish them as one of the most favorable alternatives within these emerging technologies and potential frontrunners in the quest for ITO replacements.[18]

However, integrating metal meshes into PSCs introduces specific challenges that hamper their development in comparison to other well-established PV technologies where metal mesh integration has been successful.[19,20] For example, the propensity of the halides in perovskites to penetrate thin interface layers can lead to reactions with the metal meshes, causing severe degradation in the active layer and compromising device stability.[17,21,22] To address this issue, protective layers are often introduced to prevent ion migration within the devices and maintain their performance.[23] Furthermore, perovskite layers are generally quite thin. Any imperfections or roughness on the surface of the metal mesh can have an impact on the quality of the perovskite film deposited on top.[24,25] Achieving a smooth and uniform perovskite layer on metal meshes can pose additional challenges.

In the context of PSCs, the search for novel transparent conductive materials has primarily focused on applications for flexible substrates, thus targeting bottom electrodes. In flexible devices, glass is often replaced by materials like PET (polyethylene terephthalate) or PES (polyestersulfone) due to their flexibility and lightweight properties. Although commercially available, ITO films on plastic substrates suffer from significant limitations. The first major drawback is their extreme fragility, stemming from the brittleness of ITO. Additionally, their performance falls short of that achieved with glass-based ITO films, primarily due to the constraints on annealing temperatures imposed by the use of plastic substrates.[19] This presents the need for efficient alternative solutions, and metal meshes find a suitable ground in this regard. Several works have explored the possibility of embedding metal meshes into a PET substrate employing a UV curable resin. The resulting structures are then coupled with conductive materials such as ITO, AZO or other polymers, generating a hybrid electrode.[26–31]

The integration of metal meshes into PV devices extends beyond rear electrode applications; these structures are equally well-suited as top electrodes. The adoption of a transparent or semi-transparent front contact can yield substantial improvements in solar cell performance, enabling the development of bifacial solar cells, tandem integration, and transparent photovoltaic solutions. For instance, transparent mesh front electrodes could serve as transport interlayer in multi-junction applications, enhancing performance compared to single-junction technologies.[2,32] Similarly, bifacial solar cells have demonstrated the capability to improve module power density by tens of percentages compared to their monofacial counterparts.[33] However, difficulties in fabricating high-quality structures without damaging the underlying material limits the exploration of alternative top TCEs.[34] Currently, to the authors' knowledge, there are no scientific papers that investigate the integration of metal meshes as transparent top electrodes in PSCs. Some instances have explored the use of conductive oxides/polymers, carbon nanomaterials, nanowires, and ultrathin metal films as potential alternatives.[34–37]

This work encompasses mesh integration both as bottom and top electrode, with the dual goal of finding viable alternative to commonly used TCOs and enhancing the overall performances of PSCs through bifacial and tandem integration. In contrast to prior research efforts focusing on embedded mesh structures for bottom electrode application, this study introduces an innovative rear electrode design featuring embossed metal meshes on a rigid glass substrate. This rear transparent electrode consists of photolithography gold meshes combined with a 5–10 nm thick conductive layer on top. The top electrode, usually made up of a continuous metal contact, is instead replaced by aerosol-jet printed silver meshes generating a semi-transparent or transparent front contact. **Figure 1** depicts the respective devices' architectures for both the rear and front electrode mesh integration.

2. Results and Discussion

2.1. Rear Electrode

2.1.1. Microscope Characterization of Au Meshes

The gold meshes for the rear electrode are manufactured using UV-photolithography, as detailed in Experimental Section (Section 4.1). The meshes present a grid-like structure, in which the metal lines are characterized by their linewidth (w), line thickness (t), and pitch (p), which represents the spacing between two adjacent meshes. The meshes are fabricated reproducing the pattern of commonly used ITO substrates in the lab, consisting of nine pixels (Figure 1a). Three distinct designs are employed for our study: the first one features a linewidth of 1 μm and pitch of 10 μm (referred to as 1 × 10 μm), the second one a linewidth of 2 μm and pitch of 50 μm (2 × 50 μm), and the third one a linewidth of 2 μm and pitch of 100 μm (2 × 100 μm). The thickness remains unvaried across all designs and is fixed at 100 nm.

Figure 2 displays selected images of the fabricated Au meshes using photolithography. The design and size of the structures closely adhere to the specified dimensions described earlier. In Figure 2a, the meshes appear indistinct to the human eye due to their micro-structure. Only the underlying pattern onto which the meshes are deposited is visible. To ensure better connection during *JV* measurement, it is decided to deposit the meshes exclusively onto the 9-pixel squares at the center of the substrate. In contrast, the contacts surrounding the squares are made of a continuous gold film. This design choice allows to have a better connection between the pixels and the pins of the *JV* measurement setup.

2.1.2. Benchmarking Mesh against Standard ITO Electrode

Efficient solar cell electrodes must exhibit a good balance between transparency and conductivity. Enhancing the transmittance of these structures can be achieved through geometric

© 2023 The Authors. Advanced Materials Interfaces published by Wiley-VCH GmbH

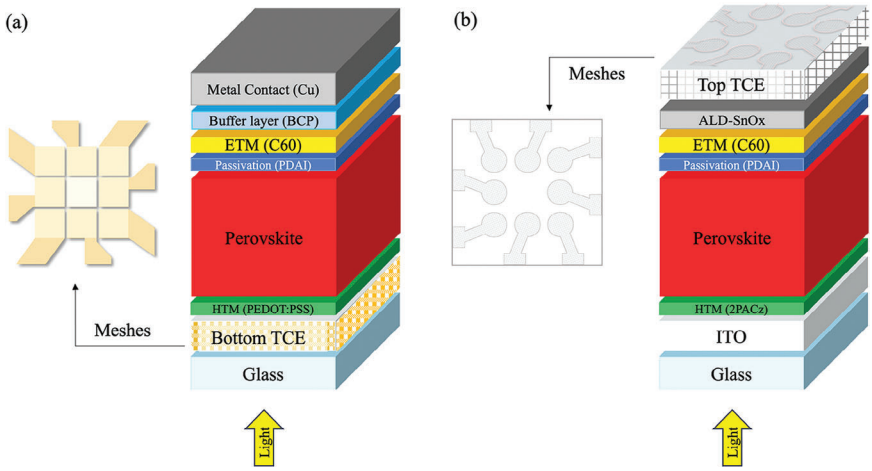


Figure 1. Cell architectures of perovskite devices for integration of a) Au meshes as bottom electrode and b) Ag meshes as top electrode.

modifications of the meshes, primarily by reducing the linewidth and increasing the pitch, which diminishes coverage. However, such alterations entail a reduction in conductivity that could impact the device's overall performance. Increasing the thickness of the meshes can linearly reduce the sheet resistance (R_s) without compromising transmittance. However, this adjustment increases the surface roughness of the electrode which may cause shunting in the thin film devices. Finding the optimal mesh design for an electrode application implies identifying the trade-off between conductivity and transparency.

The figure of merit proposed by Haacke enables quantification of this trade-off and comparison of different transparent conductive films based on their optical and electrical properties[38]; it is computed as:

$$\phi_H = \frac{T_{550\,\mathrm{nm}}^{10}}{R_{\mathrm{s,mesh}}} \left[10^{-3}\ \Omega^{-1}\right] \quad (1)$$

where $T_{550\,\mathrm{nm}}$ is the optical transmittance at 550 nm and $R_{s,\,\mathrm{mesh}}$ is the sheet resistance of the meshes, which can be approximated as:[39]

$$\mathrm{R_{s,mesh}} \approx \rho \times \frac{p}{w \times t} \quad (2)$$

w, p, and t are, respectively, the width, pitch, and thickness of the meshes, and ρ is the resistivity of the material. For gold, the resistivity is 2.44×10^{-8} Ωm.[40]

To probe these theoretical calculations of the sheet resistance of the metal meshes, two samples are fabricated with unpatterned meshes measuring 4 × 200 and 4 × 400 µm (linewidth × pitch), respectively. These meshes covered a square area and featured continuous metal contacts all around, enabling 4-point-probe measurement. Upon measurement, the observed sheet resistance values exhibited a deviation of approximately 5–10% compared to the theoretical values, deemed to be sufficiently accurate to approximate the sheet resistance of the other designs.

Table 1 presents the calculated area coverage ratio, measured total optical transmittance of the meshes, calculated $R_{s,\,\mathrm{mesh}}$, and corresponding figure of merit, compared against the standard ITO electrode.

The results demonstrate that a mesh electrode comprised solely of metal structures exhibits transmittance and sheet resistance comparable to a standard ITO electrode. Notably, the larger pitch designs, characterized by higher transmittance values, achieve a balance between transparency and conductivity which matches, and even has the potential to surpass, ITO performance.

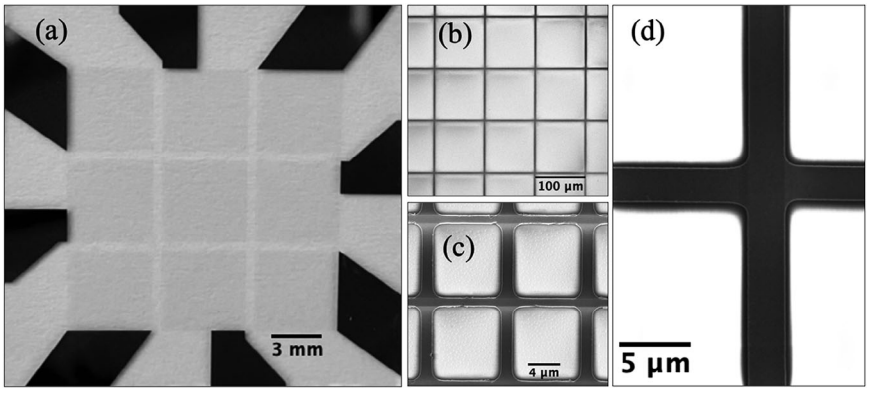


Figure 2. Representations of Au structures manufactured through photolithography: a) image of the bottom electrode contact (2 × 50 µm Au meshes not visible); b) SEM image of 2 × 100 µm meshes; c) SEM image of 2 × 10 µm meshes; d) SEM image of 2 × 50 µm meshes.

© 2023 The Authors. Advanced Materials Interfaces published by Wiley-VCH GmbH

Table 1. Area coverage ratio, transmittance at 550 nm (including glass substrate), sheet resistance and calculated Haacke's figure of merit for mesh samples identified by their linewidth × pitch, together with a standard ITO reference electrode.

	1 × 10	2 × 50	2 × 100	ITO
Coverage [%]	19	8	4	N/A
T_{550nm}[%]	68.1	81.2	86.1	88.3
R_s [Ω sq^{-1}]	2.4	6.1	12.2	15.0
Φ_H[$10^{-3}\Omega^{-1}$]	8.8	20.4	18.3	19.2

2.1.3. Current–Voltage Measurements

The 1 × 10, 2 × 50, and 2 × 100 µm mesh structures are integrated in a cell architecture as described in Figure 1a. To bridge the gaps among the meshes, reduce their surface roughness, and guarantee a more homogeneous conductivity, a 10 nm thick ITO conductive film is sputtered on top of the larger meshes designs (50 and 100 µm pitch), defining a hybrid electrode. This is deemed to play an important role in maintaining favorable optical properties while allowing efficient charge collection, compatible with the perovskite diffusion length in the 1 µm range in standard perovskite devices.[41] From the experimentally determined conductivity (1800 S cm^{-1}), we estimate the sheet resistance of the 10 nm thick ITO layer to be at least 550 Ω sq^{-1}. Such a thin interlayer shows excellent optical properties. The total transmittance of the Au meshes on glass substrate is measured at 86.1%, which only slightly decreases to 85.8% with 10 nm ITO sputtered on top of the meshes, confirming the high transparency of this thin TCO (Figure S1, Supporting Information).

Figure 3 display the *JV* curves in reverse scan of the champion devices: 1 × 10 µm (green curve), 2 × 100 µm (red curve), and 2 × 50 µm (blue curve). Note that the 2 × 50 and 2 × 100 µm structures are combined with 10 nm of ITO sputtered on top. These samples are compared against a reference device (gray dashed curve) featuring a standard ITO electrode and unvaried cell stack. The average values (over the non-shunted pixels) of the performance metrics at reverse scan can be found in **Table 2**, along with the percentage of working devices (WD). The corresponding values in forward scan can be found in Table S1, Supporting Information.

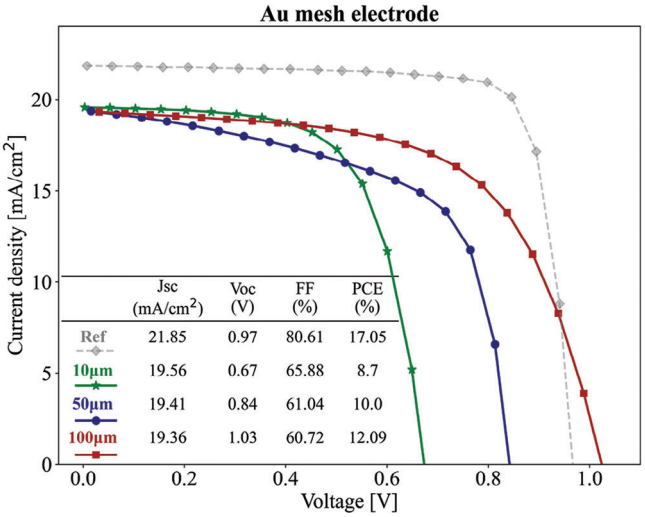


Figure 3. Reverse scan *JV* curves of champion devices: simple mesh electrode with 10 µm pitch Au meshes (green curve); hybrid electrode with 50 µm pitch Au meshes (blue curve), and 10 nm sputtered ITO layer; hybrid electrode with 100 µm pitch Au meshes (red curve) and 10 nm sputtered ITO layer; reference device with a conventional ITO electrode (gray curve).

The 1 × 10 µm mesh design, the smallest achievable with the adopted manufacturing processes, demonstrates the feasibility of charge extraction with a 10 µm spacing. Despite this distance exceeding the typical perovskite diffusion length, it is still possible to extract 75% of the generated photocurrent with respect to the reference device and achieve devices with an average efficiency of 6.1%. This ability to maintain relatively high J_{SC} can be attributed to the conductive PEDOT:PSS hole transport material (HTM), which promotes charge transfer at the electrode. In comparison to the reference device, the V_{oc} of the 1 × 10 µm pixels is notably impacted by the presence of the Au meshes, resulting in a decrease from 0.97 V in the reference to 0.6 V. This reduction may be linked to an unfavorable and/or inhomogeneous interface between the HTM and the metal meshes, leading to direct contact between the perovskite and the electrode. Such contact could serve as a non-radiative recombination center, consequently leading to a lower V_{oc}.[42,43]

Observations revealed that the 50 µm meshes, without any interlayer, resulted in notably poor performance. This may be attributed to the excessive spacing between the mesh lines, hindering the extraction of charges, even in the presence of a conducting polymer as HTM. As a result, it was determined that larger pitch structures should be combined with conductive interlayers to address this issue. With the hybrid electrode structures, the V_{oc}, together with all the other performance metrics, increases. The 2 × 100 µm sample exhibits a matching average V_{oc} with the reference, while achieving 80% of the J_{SC} extracted from the ITO electrode (Table 2). The record PCE reaches 12.1%. This enhancement can be attributed to the reduced surface roughness of the bottom electrode, resulting in a better interface with the layers above and consequently lowering the series resistance, as reported in Table S2, Supporting Information. Further optimization of the mesh design, spin coating parameters, and slightly increasing the ITO thickness, would likely narrow the performance gap with the reference devices even further.

2.2. Front Electrode

2.2.1. Microscope Characterization of Ag Meshes

Silver meshes for the front electrode are manufactured through aerosol jet printing as detailed in Experimental Section (Section 4.2). They also present a grid-like structure similar to the one employed for the Au meshes, but with a larger spacing between the metal lines. Particularly, three distinct designs are under consideration, distinguished by variations in their pitch dimensions, which are set at 0.5, 0.75, and 1 mm. The structures are positioned on the electrode so as to replicate the pattern of commonly evaporated continuous metal electrodes (Figure 1b).

© 2023 The Authors. Advanced Materials Interfaces published by Wiley-VCH GmbH

Table 2. Summary statistics for samples with Au meshes under *JV* measurements in reverse scan: sample name, percentage of working devices (WD) (out of a total of 8), average J_{sc}, average V_{oc}, average FF, average PCE. Electrode name identified by the linewidth x pitch; ITO10 indicates presence of 10 nm of sputtered ITO.

Electrode name	WD [%]	Avg. Jsc [mA cm^{-2}]	Avg. Voc [V]	Avg. FF[%]	Avg. PCE [%]
1 × 10 µm	37	15.72 ± 5.6	0.61 ± 0.08	58.74 ± 11.2	6.10 ± 3.4
2 × 50 µm, ITO10	37	18.53 ± 0.9	0.72 ± 0.1	52.63 ± 15.2	7.22 ± 3.1
2 × 100 µm, ITO10	87	17.13 ± 2.1	0.97 ± 0.1	49.55 ± 9.7	8.47 ± 2.9
Ref	75	21.11 ± 0.7	0.97 ± 0.002	79.58 ± 1.5	16.28 ± 0.7

Figure 4 presents the microscope images of the metal structures with different pitches, superimposed on a perovskite pixel. The illustrations offer a visual representation of how the the silver meshes are integrated into the solar cell architecture following the pattern in Figure 1b. The details of the meshes' designs are summarized in **Table 3**. The values of the lines' thicknesses and widths are estimated through the analysis of bright-field microscope images.

2.2.2. Assessing Impact of Laser Sintering through PL Measurements

Achieving high conductivity in the aerosol jet printed meshes requires a sintering process. The traditional thermal treatment involves heating the samples up to 250 °C, which is unsuitable for perovskite materials.[44] To overcome this limitation, laser curing is explored as an alternative method for localized sintering without subjecting the entire device to elevated temperatures. This laser treatment is found to significantly enhance the conductivity of the metal meshes, yielding similar results to traditional thermal annealing. Nevertheless, concerns arise regarding the potential impact of the laser treatment on the nearby perovskite material. While the perovskite layer is shielded by the SnO_x, there was uncertainty on whether the laser could induce local heating or cause degradation due to high-intensity radiation. To investigate this, two samples are manufactured: one with laser sintered silver meshes and another one with un-sintered ones. Both samples are then tested using photoluminescence spectroscopy (PL) with the laser being shone from the devices' glass side, in an area where both the meshes and the perovskite material are present.

The integral PL spectral mapping is plotted to detect any changes in the emissive properties of the perovskite material (**Figure 5**a,b. This is done by computing the integral of the intensity of each collected PL spectrum at a given position. The PL spectra are also analyzed to identify any visible shifts in the band gap, which could be linked to the laser treatment. To do that, the center of mass for each collected PL spectrum is computed (Figure 5c,d).

Upon inspection of the integral PL plot and centroid plot, shown in Figure 5, it appears that the laser sintering process did not cause a very significant decrease in the PL properties of the perovskite layers. Note that the higher PL intensity along the mesh pattern is attributed to the reflection of silver from the metal grids. When comparing the average PL integral values on the mesh pattern for both sintered and non-sintered samples, we observe only a 3% decrease in intensity. The average PL spectra for both the sintered and non-sintered samples, both on and outside the mesh area, can be found in Figure S2, Supporting Information. This reduction in PL intensity is considered minor, especially since these less emissive areas are localized and do not follow the integrity of the mesh lines. Furthermore, further optimization of the laser sintering process is possible, such as reducing the laser speed and/or decreasing its intensity.

The centroid plot reveals a slightly lower peak position for the sintered sample, averaging at 1.658 eV along the meshes. In contrast, the non-sintered sample displays a consistent peak position centered at 1.662 eV, concealing the mesh pattern. Nevertheless, it is important to highlight that the variance

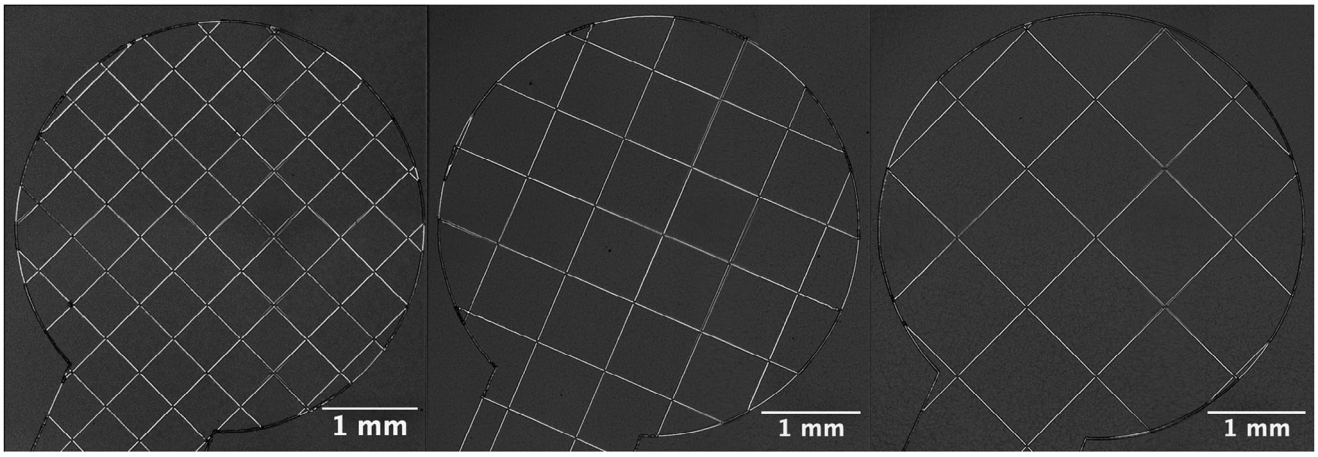


Figure 4. Microscope images of Ag meshes with different pitches on perovskite devices, from left to right: 0.5, 0.75, and 1 mm pitch.

© 2023 The Authors. Advanced Materials Interfaces published by Wiley-VCH GmbH

Table 3. Dimensions and optical properties of aerosol jet printed Ag meshes.

Pitch (p)	Thickness (t) [μm]	Line-width (d) [μm]	Coverage [%]	T_{mesh} [%]
0.5	1.8 ± 0.15	20 ± 1.5	7.84	92.16
0.75	1.8 ± 0.15	20 ± 1.5	5.26	94.74
1	1.8 ± 0.15	20 ± 1.5	3.96	96.04

in bandgap wavelength is under 1%, making it a negligible alteration. A histogram illustrating the distribution of centroid positions across the entire PL area can be found in Figure S3, Supporting Information, further corroborating the minimal disparity between the sintered and non-sintered mesh samples.

2.2.3. Performance Characterization and Assessment of Bifacial Properties

Figure 6a,b presents the *JV* characterization results of the champion devices with 1 mm-pitch Ag meshes integrated with, respectively, a Au or ITO layer on top. The thickness of the conductive films is either 5 nm (orange curves) or 10 nm (green curves). The samples are also compared with reference cells presenting a continuous Cu metal top contact (gray dashed curve). The average values for the performance metrics at reverse scan can be found in **Table 4**, along with the percentage of working devices (WD). Corresponding values for the

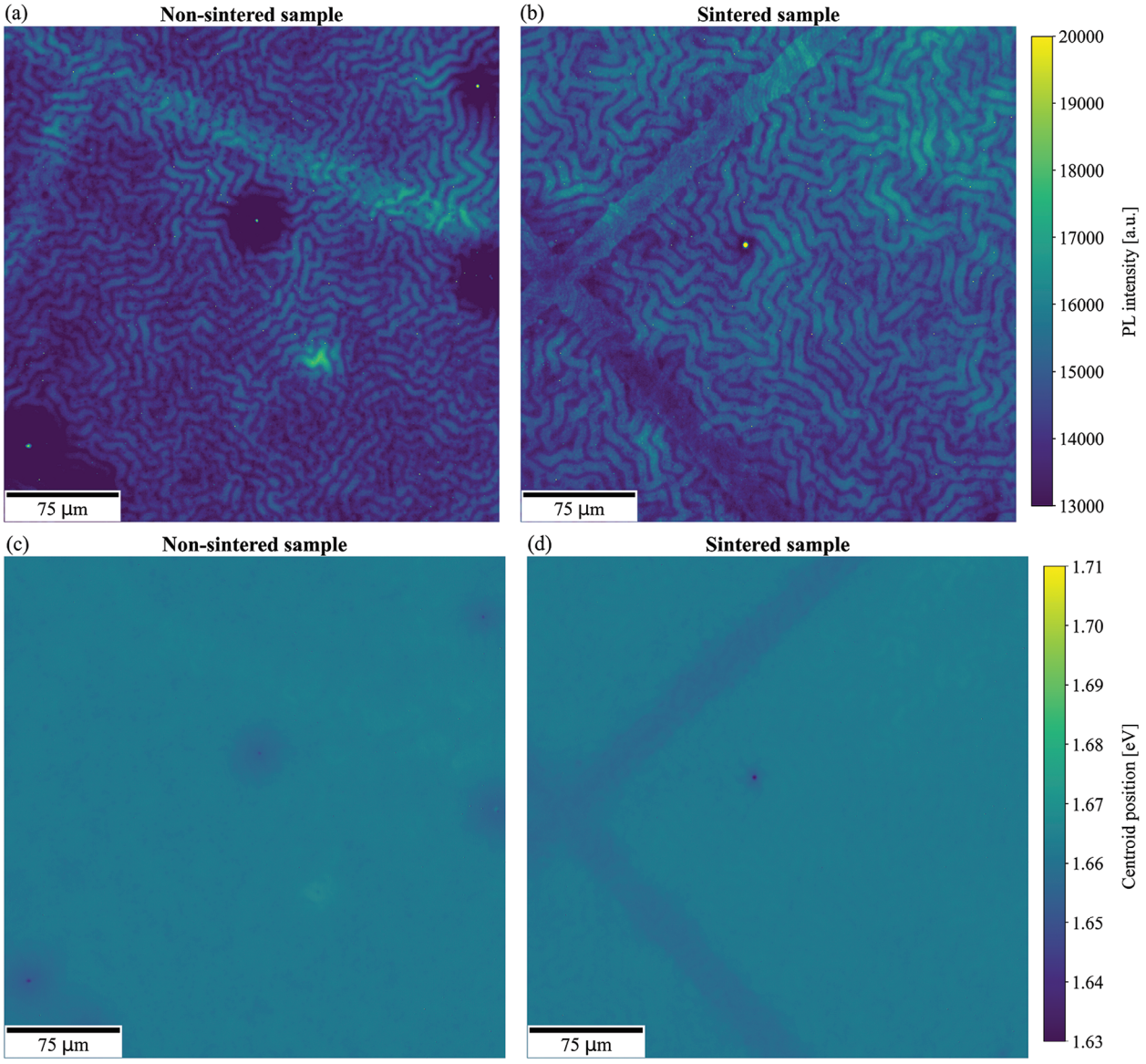


Figure 5. Hyperspectral images. a,b) Spectral integral of samples with aerosol jet-printed Ag meshes: non-sintered (a) and sintered (b). c,d) Centroid plot (center of mass of PL spectra) of samples with aerosol jet-printed Ag meshes: non-sintered (c) and sintered (d).

© 2023 The Authors. Advanced Materials Interfaces published by Wiley-VCH GmbH

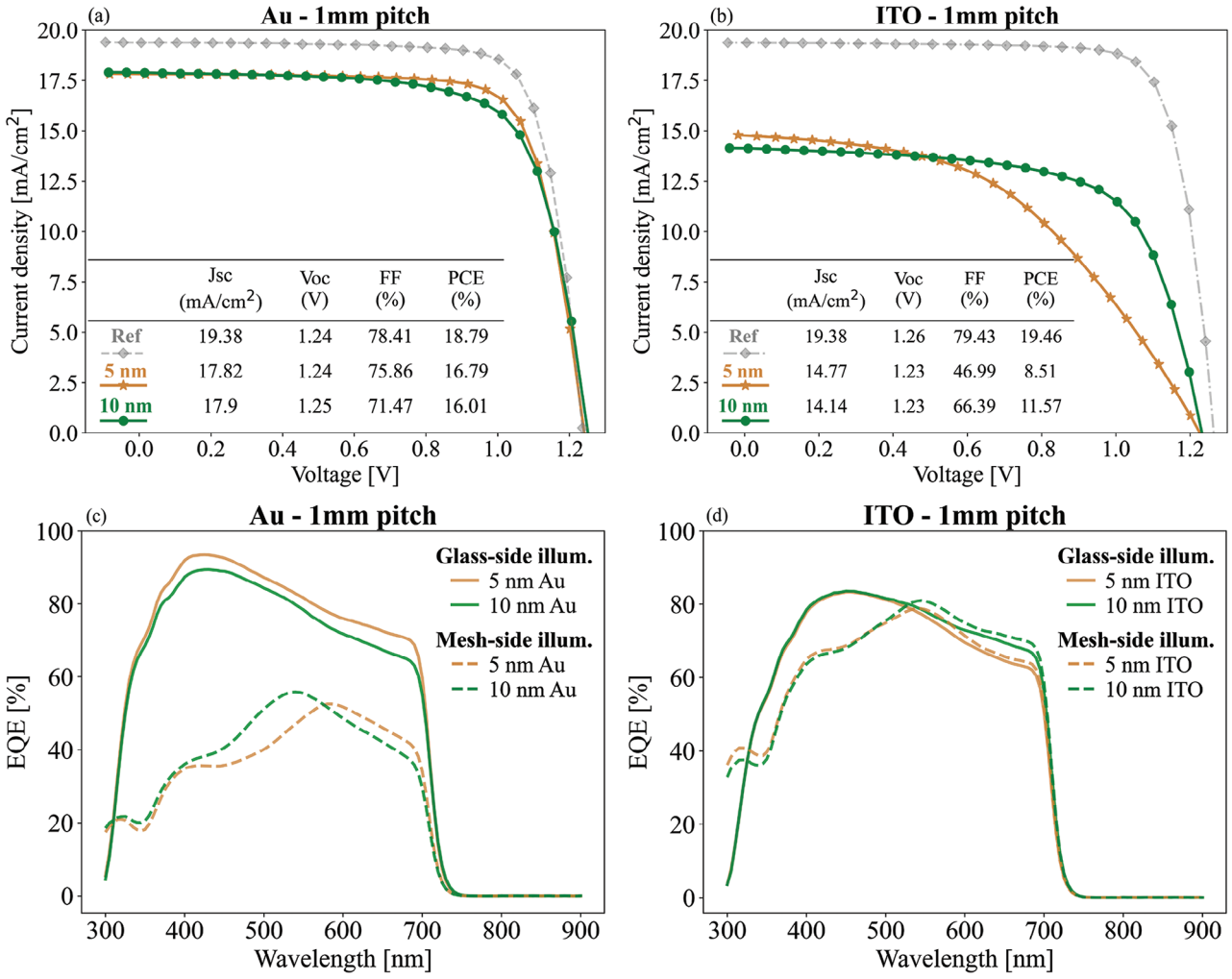


Figure 6. a,b) *JV* curves in reverse scan of the champion devices with mesh top electrode, 1 mm pitch structures, with 5-10 nm of Au (a) or ITO (b). Gray dashed curve representing the reference device with continuous Cu electrode c,d) EQE curves of representative samples with mesh top electrode, 1 mm pitch structures, with 5–10 nm of Au (c) or ITO (d). Representing performance under illumination from the glass side (solid lines) and the mesh side (dashed lines).

forward scan can be accessed in the Table S3, Supporting Information. A more graphical representation, through box-plots, of these summary statistics (both in reverse and forward scan) is also provided in Figures S4 and S5, Supporting Information.

Record performances are attained with samples featuring 5 or 10 nm Au layers, achieving PCEs of 16.8% and 16%, respectively, which are only approximately 15% lower than the reference device (PCE of 18.8%). It is noteworthy that, despite the best efficiency achieved with 5 nm of Au, a notable degree of

Table 4. Summary statistics for samples with Ag meshes under *JV* measurements in reverse scan: sample name, percentage of working devices (WD) (out of a total of 8), average J_{sc}, average V_{oc}, average FF, average PCE. Electrode name identified by the pitch dimension of Ag meshes; Au5/Au10/ITO5/ITO10 indicate presence of 5 or 10 nm of Au/ITO.

Electrode name	WD [%]	Avg. Jsc [mA cm^{-2}]	Avg. Voc [V]	Avg. FF [%]	Avg. PCE [%]
1 mm, Au5	50	17.32 ± 0.9	1.19 ± 0.06	64.54 ± 11.9	13.52 ± 3.7
1 mm, Au10	50	17.53 ± 0.4	1.23 ± 0.03	69.11 ± 2.1	14.93 ± 1.1
Ref Au	87	18.89 ± 0.3	1.23 ± 0.009	76.60 ± 1.6	17.86 ± 0.7
1 mm, ITO5	75	13.42 ± 1.2	1.24 ± 0.01	36.50 ± 7.9	6.16 ± 1.8
1 mm, ITO10	87	13.50 ± 1.7	1.15 ± 0.2	44.22 ± 12.4	7.19 ± 3.1
Ref ITO	100	18.80 ± 0.4	1.25 ± 0.02	76.60 ± 4.4	18.00 ± 1.3

© 2023 The Authors. Advanced Materials Interfaces published by Wiley-VCH GmbH

Table 5. J_{SC} calculated from EQE measurements for both glass-side and mesh-side illumination.

	$J_{SC,\ glass}$ [mA cm^{-2}]	$J_{SC,\ mesh}$ [mA cm^{-2}]
5 nm Au	17.1	9.1
10 nm Au	16.3	9.5
5 nm ITO	15.4	14.7
10 nm ITO	15.9	15.3

variability is observed among the measured pixels, which also explains the low percentage of working devices. SEM examination of the samples with evaporated gold revealed that the 5 nm Au layer is non-conformal, displaying features that indicate incomplete surface coverage. In contrast, the 10 nm thick samples exhibit a more uniform film, resulting in enhanced measurement consistency and a narrower distribution (Figure S6, Supporting Information).

Devices with ITO as the conductive layer in the hybrid electrodes generally led to inferior performance compared to their Au counterparts. This disparity in performance can be ascribed to the inherent differences in the conductive properties of the materials. While ITO is recognized for its excellence as a transparent conductor, it still presents lower conductivity when compared to metals like gold. Such thin layers of ITO may not provide adequate charge extraction, leading to elevated series resistances, as demonstrated by the R_s values in Table S4, Supporting Information, consequently resulting in a decrease in FF.

The samples exhibit consistent results across different pitch sizes, as detailed in Figure S7, Supporting Information. The absence of substantial performance improvements with narrower pitch sizes suggests that a 1 mm pitch may be sufficient for functional devices with performance levels comparable to the reference. In cases where similar outcomes are achieved, the larger pitch design is preferred for its superior transmittance and reduced material consumption.

To provide evidence of the bifacial properties of the cells equipped with the mesh top, contact EQE measurements from the meshes and glass side are carried out. Figure 6c,d showcases the EQE curves of a representative pixel for the samples with 1 mm pitch structures and variable Au and ITO thicknesses. The spectra for the remaining samples can be found in Figure S8, Supporting Information.

From the EQE values, it is also possible to compute the photocurrent density listed in **Table 5**.

The obtained results indicate that the performance reduction between the glass and mesh sides is more significant in the samples with a Au film. This is due to the opacity of the Au layer, with a measured transmittance at 550 nm of 46%, which hinders the transmission of light through the device. On the other hand, the samples with ITO show relatively consistent results when measured from both the front and front sides. The short-circuit current reduction for both ITO samples, when measured from the glass and mesh sides (Table 5), is approximately 4%. These values align well with the coverage of the 1 mm lines, as described in Table 3. This suggests that the observed decrease in J_{SC} can be attributed to the coverage of the Ag meshes, which leads to reduced light absorption and current extraction.

Overall, the incorporation of a Au interlayer is found to enhance electrical properties of the mesh samples, whereas ITO enhances bifacial characteristics. Despite recognized potential for further improvement in electrical performance by augmenting the thickness of the ITO layer, such an approach contradicts the overarching objective of minimizing indium consumption and striving toward the production of indium-free devices. Moreover, the integration of ITO into devices introduces challenges for potential applications involving flexible substrates, due to the brittleness of the material. This is also pertinent in the context of aerosol jet-printed meshes, which demonstrate high potential for flexible substrate applications. These considerations prompt the exploration of alternative materials to ITO as transparent conductive interlayers. Within this research framework, the emphasis has been put on Au; however, exploration of other transparent conductive materials such as AZO or MXenes could also open promising avenues.[25,45]

2.3. Comparison of Mesh Electrodes

The integration of metal meshes into the front and back electrodes of PSCs serves distinct functions tailored to specific goals. For the bottom Au mesh contact, the aim is to replace the conventional ITO electrode, addressing concerns related to its environmental impact, efficiency losses during upscaling, and supply risks associated with indium. The Ag top mesh contact integration seeks to enhance the overall performance of devices by enabling bifacial or multi-junction applications.

This duality in application is reflected in the choice of materials and manufacturing techniques for the metal meshes. For the rear electrode, gold is preferred due to its compatibility with perovskite material. Employing UV-photolithography, smaller mesh patterns are crafted, striking a delicate balance between high conductivity and transparency. This balance is particularly crucial in p-i-n devices, where the rear electrode allows incident radiation to pass through. For the top electrode, silver is an alternative to gold due to the absence of direct contact between the perovskite layer and the top electrode, preventing any possible ion migration. Therefore, here, silver meshes, with their higher conductivity and cost-effectiveness, become the preferred choice.[46,47] Aerosol jet printing allows for the fabrication of larger mesh structures with line thickness about 20 times bigger than with photolithography, keeping the sheet resistance sufficiently low. The locally applied laser curing step permits a successful sintering process preserving the perovskite stack beneath.

The challenges involved in the mesh integration into PSCs are many fold. In the case of gold meshes, the current deposition techniques require spincoating of the HTM and perovskite material on top of the structures. The inherent surface roughness of the substrate complicates the uniform deposition of these thin layers on the mesh electrode, leading to the formation of potential pinholes. The introduction of a 10 nm-thick layer of ITO sputtered onto the meshes offers an improved interface that reduces the risk of shunting. This hybrid electrode design achieves a significant 90% reduction in indium usage compared to a conventional perovskite stack employing a 100 nm-thick ITO substrate. Increasing the thickness of the conductive oxide could promote the formation of a defect-free interface, potentially enhancing

© 2023 The Authors. Advanced Materials Interfaces published by Wiley-VCH GmbH

device performance even further. However, to maintain the advantages of a mesh electrode over a standard ITO one, it is advisable, instead, to explore integration with alternative indium-free materials.

While the thickness of the lines in the front electrode mesh structures is not constrained by the need for spin coating on top of them, fabrication challenges still arise due to the presence of the perovskite stack beneath the metal meshes and the requirement for a sintering process. To address these issues, a thin layer of ALD SnO_x is applied to the electron transport material (ETM). This protective layer serves a dual purpose: shielding the perovskite from potential ion migration and ensuring the integrity of the perovskite stack during the laser curing process.

3. Conclusion

To attain sustainable solar cell manufacturing on a terawatt scale, the exploration of indium-free TCEs is essential. This study focused on the potential replacement of conventional ITO rear electrode and traditional metal top contacts with mesh electrodes, enabling the creation of transparent or semi-transparent solar devices.

Photolithography embossed Au meshes, utilized as bottom electrodes on glass substrates, have showcased their capability as TCEs in standalone and hybrid configurations. These structures, when paired with a 10 nm-thick ITO interlayer, have achieved promising efficiencies of up to 12%, with the extracted current surpassing 80% of that attained with a standard ITO electrode. Aerosol jet-printed Ag meshes were introduced to replace continuous metal contacts in PSCs. The experiments revealed that the perovskite material remained well-preserved even after laser sintering. Devices featuring Ag meshes combined with a thin Au layer exhibited promising performances, achieving up to 16.8% efficiency with a modest reduction of less than 10% in J_{SC} compared to the reference device employing a copper electrode. This configuration also offered moderate bifacial properties, enhancing overall device performance. Hybrid structures composed of Ag meshes and a thin ITO layer, despite the limited conductivity of the thin TCO, achieved a record efficiency of 11.6% and extracted 70% of the J_{SC} achieved by the reference device. This configuration holds even higher potential for bifacial and multijunction applications.

With continued optimization, such as modifications of the mesh design, tuning of the spin-coating parameters, interface engineering, and choice of alternative transparent conductive materials, mesh electrodes hold great promise for advancing the development of sustainable and efficient photovoltaic devices.

4. Experimental Section

UV-Photolithography for Bottom Electrode: Manufacturing of metal meshes began by cleaning twice 4″ and 550 µm-thick soda lime glass (SLG) wafers at 100 °C in a Piranha solution, which is a 3:1 solution of strong sulfuric acid (H_2SO_4) and hydrogen peroxide (H_2O_2). The wafers were then spin coated with the negative photoresist AZ nLOF 2020 using a Süss ACS200 GEN3 modular cluster tool. After UV exposure through direct laser writing, the samples were developed with the same cluster tool. Following development, any leftover residues were removed through high-frequency O_2 plasma cleaning for 10 s at 200 W (Tepla-Z2). Gold metal films were then deposited using a Leybold Optics LAB 600H through e-beam evaporation. A thin layer of 10 nm of titanium (Ti) was deposited first to favor adhesion, followed by gold. Finally, the photoresist lift-off process took place thanks to remover 1165 revealing the wanted mesh structure on the glass wafer.

For the small mesh design (1 × 10 µm), due to the particularly tight structures, a positive photoresist, LOR 5A 400 nm + AZ 1512 HS 1.1 µm, was employed. The utilization of these different photoresists allowed for a successful lift-off process, enabling the remover to etch the desired parts of the meshes.

Aerosol Jet Printing for Front Electrode: The silver meshes were printed through an aerosol jet printer (Opamec Decathlon AJ-5X) with a nozzle of size 100 µm using the Novacentrix JS-ADEV N250 silver nanoparticle ink. During printing, the subtrate was heated to 80 °C to ensure fast fast evaporation of the ink's solvent. Right after printing, the structures underwent a laser sintering process, with the laser spot following the printed paths, offering a localized annealing treatment. This process used a 830 nm (NIR) laser with a power of 680 mW (2486-L4 from JDSU). Both processes, printing, as well as laser sintering, were run at 4 mm s^{-1}.

Hybrid Electrodes: Mesh structures both in the front and rear electrode were integrated with thin conductive layers, consisting of ITO or Au. Thin layers of ITO, either 5 or 10 nm-thick, were sputtered onto the meshes. In both electrodes, the oxide was sputtered solely in alignment with the pixels to prevent any risk of short-circuiting. For the front electrode, this was achieved with a ink pen used to draw lines for pixel separation. Following the sputtering, the sacrificial layers, defined by the pen, were dissolved in acetone using an ultrasonic bath for a brief duration. For the front contact, a metal mask was used to pattern the electrode.

ITO was sputtered with a home-built setup in the class 10 000 clean room. The ITO target was In_2O_3/SnO_2 90/10 wt%, used with an argon flow of 20 sccm, pressure of 6.67×10^{-3} mbar, and power of 20 W in RF mode. The deposition rate was 2 nm min^{-1}, resulting in an ITO conductivity of 1800 S cm^{-1}, measured with a 4-point-probe.

A thin layer of gold, either 5 or 10 nm-thick, was also explored as alternative to ITO in the bottom hybrid electrode. Such a layer was thermally evaporated using a metal mask.

Perovskite Solar Cell Fabrication: The experiments focused on widegap p-i-n devices known as formamidinium (FA) cesium-based devices, specifically $FA_{0.75}Cs_{0.25}PbI_{2.4}Br_{0.6}$. The perovskite material featured a band gap of approximately 1.67 eV and low bromide content (30%). Solution-based processing was utilized for both the HTM and the perovskite active layer. Thermal evaporation was employed for the ETM, passivation layer, and the continuous metal front contact. Manufacturing of cells was carried out in batches of nine devices each presenting eight working pixels. The steps involved in the manufacturing process are herein described.

The HTM, perovskite, and passivation layers were spin coated onto the substrate. In the case of the rear contact integration, this substrate comprised a hybrid Au mesh electrode. For the front electrode, it consisted of a standard 1-inch, pre-patterned 100 nm-thick ITO layer on soda lime glass (SLG). Prior to use, the ITO substrate underwent a thorough cleaning process, involving several steps: First, it was subjected to a 15-min ultrasonic bath in a 2% Decon 90 solution in deionized water, followed by rinsing with deionized water and another 5-min ultrasonic bath. Next, the substrate was immersed in acetone for 15 min using an ultrasonic bath, and then in IPA for another 15 min. Finally, it was dried using compressed air and subjected to a 15-min UV/ozone treatment.

HTM: Two different HTM were employed in this study: PEDOT:PSS and 2PACz. While PEDOT:PSS was used for the devices with a meshed bottom electrode, 2PACz was preferred for the front electrode integration. This choice was determined by the unfavorable interface between this HTM and the Au meshes, which is, instead, improved with PEDOT:PSS. The 2PACz HTM consisted of a 1.5 mM solution of 2PACz in anhydrous ethanol. Previous to spin coating at 3000 rpm (5 s ramp) for 30 s, the 2PACz was sonicated for 15 min. 100 mL per device was dispensed

© 2023 The Authors. Advanced Materials Interfaces published by Wiley-VCH GmbH

onto each sample. It was then annealed on a hot plate at 100 °C. PEDOT:PSS was purchased from Ossila (Al 4083) and diluted with methanol in a 3:1 ratio and sonicated before use. The solution was filtered using a 0.45 µm PTFE filter and spread on the substrate. After spin coating (4000 rpm, 1000 rpm ramp, 30s), the substrate was heated to 120 °C for 20 min.

PVK: The perovskite active layer consisted of a 1.1 M solution of $FA_{0.75}Cs_{0.25}PBI_{2.4}Br_{0.6}$, which was prepared by dissolving 0.825 M of formamidinium iodide (FAI, Greatcell Solar), 0.275 M of cesium iodide (CsI, Sigma-Aldrich), 0.33 M of lead bromide (PbBr2, TCI), and 0.781 M of lead iodide (PbI2, TCI) in a 4:1 (vol:vol) mixture of N,N-dimenthylformamide (Sigma-Aldrich) and dymethylsulfoxide (Sigma-Aldrich). The solution was then stirred at 50 °C until fully dissolved (about 2 h). Before spin coating, the solution was filtered with a PTFE 0.22 µm filter. Each device was spread with 100 µL of perovskite solution and spin coated for 10 s at 2000 rpm and for 40 s at 6000 rpm. 20 s prior to the end of the program, 200 µL of antisolvant chlorobenzene (CB) was dispensed on the sample to favor crystallization. The samples were then transferred to a hot plate and annealed for 30 min at 100 °C.

PDAI: A 0.3 mg mL^{-1} solution of PDAI (Sigma-Aldrich) in a 1:1 (vol:vol) mixture of isopropanol and toluene was stirred at 70 °C for 2 h. The solution was then filtered through a 0.22 µm PTFE filter, and 100 mL per device was spin coated at 4000 rpm for 20 s, followed by annealing at 100°C for 5 min.

The ETM was deposited through thermal evaporation in vacuum; 20 nm of C_{60} (Sigma-Aldrich) was evaporated on top of the PDAI. The same procedure was applied for the 7 nm of bathocuproine (Sigma-Aldrich) and 120 nm of copper for the devices featuring meshes as bottom electrodes. The devices with mesh front electrode do not present these two last layers but are instead substituted by ALD SnO_x.

A 25 nm SnO_x interlayer was deposited by atomic layer deposition (Picosun). Tetrakis(dimethylamino)tin(IV) (TDMASn, EpiValence) was used as precursor and H_2O as a reactant. The precursor bubbler was heated to 75 °C and the chamber to 100 °C. The reactant vessel was kept at room temperature. The pulsing sequence consisted of a 0.6 s pulse of TDMASn, 30 s purge, 0.1 s pulse of H_2O, and 30 s purge, resulting in a growth rate of 0.1 nm per cycle.

Sample Characterization: *JV* measurements were conducted using an Arkeo multichannel platform (Cicci Research) and an LED solar simulator (G2V Sunbrick Base-UV). The devices' active area was 0.158 cm^2. Scanning was performed in both forward and reverse directions at a scan rate of 200 mV s^{-1} with a voltage step of 50 mV. The samples were placed on a custom-made sample holder equipped with pins for easy connection to the devices.

For EQE measurements, a Bentham PVE300 system in transformer mode was used. The light source consisted of a dual xenon short-arc lamp and a quartz halogen lamp. A 10 × 10 mm Si reference cell was employed to calibrate the power of the probe beam.

Wide-field hyperspectral photoluminescence (PL) measurements were carried out on a Photon Etc IMA Vis system. The samples were illuminated with a 405 nm continuous wave laser through a 20x chromatic aberration corrected objective lens (Nikon TU Plan Fluor, 0.45 NA). The illumination was structured to have a uniform top hat profile across an area larger than the collected images are collected from (330 × 330 μm^2). The monochromatic illumination intensity was measured to be 65 mW cm^{-2}, approximately 1 sun equivalent for materials with the bandgap used in this work. PL was collected through the same objective lens, spectrally split through a volume Bragg grating before the image was focused onto a digital CMOS camera (Hamamatsu ORCA-Flash4.0 V3)

For spectroscopy measures, total transmittance and total reflectance spectra were acquired through a Shimadzu UV-3600Plus UV–vis spectrometer with the Shimadzu ISR-603 integrating sphere.

Supporting Information

Supporting Information is available from the Wiley Online Library or from the author.

Acknowledgements

The authors acknowledge the Engineering and Physical Sciences Research Council (EPSRC, EP/T02030X/1, EP/V027131/1, EP/S01781X/1) for funding. S.D.S. acknowledges the Royal Society and Tata Group (grant no. UF150033). The work has received funding from the European Research Council under the European Union's Horizon 2020 research and innovation program (HYPERION, grant agreement no. 756962). Part of this work was undertaken using equipment facilities provided by the Henry Royce Institute, via the grant Henry Royce Institute, Cambridge Equipment: EP/P024947/1 and EP/R00661X/1, with additional funding from the "Centre for Advanced Materials for Integrated Energy Systems (CAM-IES)" (EP/P007767/1). The authors would also like to express their gratitude to the SFA-AM SCALAR project, who funded part of the research. Finally, sincere thanks are also extended to Yang Lu, Melissa Fitzsimmons, and Krishna Manwani for their contributions and experimental support to this work. For the purpose of open access, the authors have applied a Creative Commons Attribution (CC BY) license to any Author Accepted Manuscript version arising from this submission.

Conflict of Interest

The authors declare no conflict of interest.

Data Availability Statement

The data that support the findings of this study are available from the corresponding author upon reasonable request.

Keywords

aerosol jet printing, metal meshes, perovskite solar cells, transparent conducting electrodes, UV-photolithography

Received: November 1, 2023
Revised: November 18, 2023
Published online:

[1] V. Ramasamy, J. Zuboy, E. O'Shaughnessy, D. Feldman, J. Desai, M. Woodhouse, P. Basore, R. Margolis, U.S. Solar Photovoltaic System and Energy Storage Cost Benchmarks, With Minimum Sustainable Price Analysis, **2022**, https://www.osti.gov/biblio/1891204.
[2] Best research-cell efficiency chart, https://www.nrel.gov/pv/assets/pdfs/best-research-cell-efficiencies.pdf (accessed: July 2023).
[3] M. J. Kerr, A. Cuevas, P. Campbell, *Progress in Photovoltaics: Research and Applications* **2003**, *11*, 97.
[4] N. M. Haegel, P. Verlinden, M. Victoria, P. Altermatt, H. Atwater, T. Barnes, C. Breyer, C. Case, S. De Wolf, C. Deline, M. Dharmrin, B. Dimmler, M. Gloeckler, J. C. Goldschmidt, B. Hallam, S. Haussener, B. Holder, U. Jaeger, A. Jaeger-Waldau, I. Kaizuka, H. Kikusato, B. Kroposki, S. Kurtz, K. Matsubara, S. Nowak, K. Ogimoto, C. Peter, I. M. Peters, S. Philipps, M. Powalla, et al., *Science* **2023**, *380*, 39.
[5] Iea_net_zero_by_2050.pdf, https://unfccc.int/sites/default/files/resource/IEA_net_zero_by_2050.pdf (accessed: July 2023).
[6] W. Zhang, G. E. Eperon, H. J. Snaith, *Nat. Energy* **2016**, 1.
[7] G. Hodes, *Science* **2013**, *342*, 317.
[8] S. D. Stranks, H. J. Snaith, *Nat. Nanotechnol.* **2015**, *10*, 391.
[9] S. D. Stranks, *Contemp. Phys.* **2023**, *63*, 280.
[10] D. Li, D. Zhang, K.-S. Lim, Y. Hu, Y. Rong, A. Mei, N.-G. Park, H. Han, *Adv. Funct. Mater.* **2021**, *31*, 2008621.

© 2023 The Authors. Advanced Materials Interfaces published by Wiley-VCH GmbH

[11] P. P. Edwards, A. Porch, M. O. Jones, D. V. Morgan, R. M. Perks, *Dalton Trans.* **2004**, *19*, 2995.
[12] D. Bauer, D. Diamond, J. Li, D. Sandalow, P. Telleen, B. Wanner, U.S. Department of Energy Critical Materials Strategy. United States, https://doi.org/10.2172/1000846.
[13] J. Gong, S. B. Darling, F. You, *Energy Environ. Sci.* **2015**, *8*, 1953.
[14] A. Kumar, C. Zhou, *ACS Nano* **2010**, *4*, 11.
[15] Y. Zhang, M. Kim, L. Wang, P. Verlinden, B. Hallam, *Energy Environ. Sci.* **2021**, *14*, 5587.
[16] S. Sharma, S. Shriwastava, S. Kumar, K. Bhatt, C. C. Tripathi, *Opto-Electronics Review* **2018**, *26*, 223.
[17] D. Zhang, A. H. Alami, W. C. Choy, *Solar RRL* **2022**, *6*, 2100830.
[18] J. Fleury, L. Brunier, M. Lagier, S. Shukla, K. Manwani, E. Panda, A. Schüler, *Sol. Energy Mater. Sol. Cells* **2023**, *257*, 112345.
[19] P. Bellchambers, C. Henderson, S. Abrahamczyk, S. Choi, J.-K. Lee, R. A. Hatton, *Adv. Mater.* **2023**, *35*, 2300166.
[20] J. Zhu, X. Zhu, R. Hoekstra, L. Li, F. Xiu, M. Xue, B. Zeng, K. L. Wang, *Appl. Phys. Lett.* **2012**, *100*, 14.
[21] J. Kang, K. Han, X. Sun, L. Zhang, R. Huang, I. Ismail, Z. Wang, C. Ding, W. Zha, F. Li, et al., *Org. Electron.* **2020**, *82*, 105714.
[22] K. Domanski, J.-P. Correa-Baena, N. Mine, M. K. Nazeeruddin, A. Abate, M. Saliba, W. Tress, A. Hagfeldt, M. Grätzel, *ACS Nano* **2016**, *10*, 6306.
[23] Z. Xiao, Y. Yuan, Y. Shao, Q. Wang, Q. Dong, C. Bi, P. Sharma, A. Gruverman, J. Huang, *Nat. Mater.* **2015**, *14*, 193.
[24] P. Holzhey, M. Prettl, S. Collavini, C. Mortan, M. Saliba, *Sci. Rep.* **2023**, *13*, 6375.
[25] J. Mohanraj, C. R. Singh, T. P. Gujar, C. D. Heinrich, M. Thelakkat, *Nanomaterials* **2021**, *11*, 1783.
[26] H. Ji, J. Huang, W. Zhang, X. Chen, Y. Lu, C. Ding, J. Fang, W. Song, L. Ai, *Adv. Mater. Interfaces* **2022**, *9*, 2200483.
[27] Z. Zhong, P. Ko, H. Youn, A. Kim, K. Woo, *International Journal of Precision Engineering and Manufacturing-Green Technology* **2021**, 1.
[28] L. Mao, Q. Chen, Y. Li, Y. Li, J. Cai, W. Su, S. Bai, Y. Jin, C.-Q. Ma, Z. Cui, L. Chen, *Nano Energy* **2014**, *10*, 259.
[29] J. Wang, X. Chen, F. Jiang, Q. Luo, L. Zhang, M. Tan, M. Xie, Y.-Q. Li, Y. Zhou, W. Su, Y. Li, C.-Q. Ma, *Solar RRL* **2018**, *2*, 1800118.
[30] Y. Li, L. Meng, Y. Yang, G. Xu, Z. Hong, Q. Chen, J. You, G. Li, Y. Yang, Y. Li, *Nat. Commun.* **2016**, *7*, 10214.
[31] R. Schneider, P. A. Losio, F. A. Nüesch, J. Heier, *Int. J. Adv. Des. Manuf. Technol.* **2019**, *103*, 3901.
[32] N. N. Lal, Y. Dkhissi, W. Li, Q. Hou, Y.-B. Cheng, U. Bach, *Adv. Energy Mater.* **2017**, *7*, 1602761.
[33] R. Guerrero-Lemus, R. Vega, T. Kim, A. Kimm, L. Shephard, *Renewable Sustainable Energy Rev.* **2016**, *60*, 1533.
[34] Y. Xu, Z. Lin, W. Wei, Y. Hao, S. Liu, J. Ouyang, J. Chang, *Nano-Micro Lett.* **2022**, *14*, 117.
[35] J.-G. Kim, S.-I. Na, H.-K. Kim, *AIP Adv.* **2018**, *8*, 10.
[36] C. Xu, X. Zhao, J. Ma, J. Guo, T. Ma, M. Wu, *ChemElectroChem* **2021**, *8*, 4396.
[37] T.-Y. Jin, W. Li, Y.-Q. Li, Y.-X. Luo, Y. Shen, L.-P. Cheng, J.-X. Tang, *Adv. Opt. Mater.* **2018**, *6*, 1801153.
[38] G. Haacke, *J. Appl. Phys.* **1976**, *47*, 4086.
[39] J. Hautcoeur, X. Castel, F. Colombel, R. Benzerga, M. Himdi, G. Legeay, E. Motta-Cruz, *Thin Solid Films* **2011**, *519*, 3851.
[40] J. Baptiste, Resistivity of gold—The physics factbook, https://hypertextbook.com/facts/2004/JennelleBaptiste.shtml (accessed: July 2023).
[41] S. D. Stranks, G. E. Eperon, G. Grancini, C. Menelaou, M. J. Alcocer, T. Leijtens, L. M. Herz, A. Petrozza, H. J. Snaith, *Science* **2013**, *342*, 341.
[42] U. Rau, *Phys. Rev. B* **2007**, *76*, 085303.
[43] I. L. Braly, D. W. DeQuilettes, L. M. Pazos-Outón, S. Burke, M. E. Ziffer, D. S. Ginger, H. W. Hillhouse, *Nat. Photonics* **2018**, *12*, 355.
[44] X. Meng, X. Tian, S. Zhang, J. Zhou, Y. Zhang, Z. Liu, W. Chen, *Solar RRL* **2022**, *6*, 2200280.
[45] T. Guo, D. Zhou, S. Deng, M. Jafarpour, J. Avaro, A. Neels, J. Heier, C. Zhang, *ACS Nano* **2023**, *17*, 3737.
[46] Electrical conductivity—Elements and other materials, https://www.engineeringtoolbox.com/conductors-d_1381.html (accessed: July 2023).
[47] Gold & silver price charts - live prices| goldsilver.com| goldsilver.com, https://goldsilver.com/price-charts/ (accessed: July 2023).

© 2023 The Authors. Advanced Materials Interfaces published by Wiley-VCH GmbH